Published in final edited form as:
Contact (Thousand Oaks). 2018 September 24; 1(1): 1–14. doi:10.1177/2515256418801423.

Ultrastructural Characterization of Flashing Mitochondria

Manon Rosselin[1], **Paula Nunes-Hasler**[1], and **Nicolas Demaurex**[1,iD]

[1]Department of Cell Physiology and Metabolism, University of Geneva, Switzerland

Abstract

Mitochondria undergo spontaneous transient elevations in matrix pH associated with drops in mitochondrial membrane potential. These *mitopHlashes* require a functional respiratory chain and the profusion protein optic atrophy 1, but their mechanistic basis is unclear. To gain insight on the origin of these dynamic events, we resolved the ultrastructure of flashing mitochondria by correlative light and electron microscopy. HeLa cells expressing the matrix-targeted pH probe mitoSypHer were screened for mitopHlashes and fixed immediately after the occurrence of a flashing event. The cells were then processed for imaging by serial block face scanning electron microscopy using a focused ion beam to generate ~1,200 slices of 10 nm thickness from a 28 µm × 15 µm cellular volume. Correlation of live/fixed fluorescence and electron microscopy images allowed the unambiguous identification of flashing and nonflashing mitochondria. Three-dimensional reconstruction and surface mapping revealed that each tomogram contained two flashing mitochondria of unequal sizes, one being much larger than the average mitochondrial volume. Flashing mitochondria were 10-fold larger than silent mitochondria but with a surface to volume ratio and a cristae volume similar to nonflashing mitochondria. Flashing mitochondria were connected by tubular structures, formed more membrane contact sites, and a constriction was observed at a junction between a flashing mitochondrion and a nonflashing mitochondrion. These data indicate that flashing mitochondria are structurally preserved and bioenergetically competent but form numerous membrane contact sites and are connected by tubular structures, consistent with our earlier suggestion that mitopHlashes might be triggered by the opening of fusion pores between contiguous mitochondria.

Keywords

membrane contact sites; mitochondrial dynamics; bioenergetics; electron microscopy; fluorescence microscopy; correlative light and electron microscopy

[iD]**ORCID iD**
Nicolas Demaurex http://orcid.org/0000-0002-9933-6772

Corresponding Author: Nicolas Demaurex, Department of Cell Physiology and Metabolism, University of Geneva, 1 Rue Michel-Servet, Geneva 1211, Switzerland. Nicolas.Demaurex@unige.ch.

Declaration of Conflicting Interests
The author(s) declared no potential conflicts of interest with respect to the research, authorship, and/or publication of this article.

Europe PMC Funders Author Manuscripts

Introduction

Mitochondria consume most of the oxygen on our planet to generate ATP by oxidative phosphorylation. This fundamental process involves the bidirectional transfer of protons across the inner mitochondrial membrane. Protons are expelled from the matrix into cristae along the electron transport chain (respiratory Complexes I to IV) to generate a proton-motive force (Δp) composed of an electrical component, the mitochondrial membrane potential, $\Delta\psi_m$, negative inside, and of a chemical component, the transmembrane pH gradient, ΔpH_m, alkaline inside. The electrical and chemical components add up to drive the reverse flux of protons across the ATP synthase (Complex V), which generates ATP in the mitochondrial matrix. This proton circuit is central to the Mitchell's (1961) chemiosmotic theory of ATP synthesis.

In living cells and tissues, mitochondria display abrupt transient elevations in matrix pH associated with drops in $\Delta\psi_m$. These mitochondrial *flashes* were initially proposed to reflect changes in superoxide anions (W. Wang et al., 2008), but the reporter probe, a circularly permutated yellow fluorescent protein, was subsequently shown to be unresponsive to superoxide and highly sensitive to pH (Schwarzlander et al., 2014). Circularly permutated yellow fluorescent protein flashes correspond to ~0.4 pH reversible alkalinizations of the mitochondrial matrix that can be recorded with a range of structurally unrelated pH probes targeted to the mitochondrial matrix (Rosselin, Santo-Domingo, Bermont, Giacomello, & Demaurex, 2017). We therefore termed these dynamic events mitopHlashes to emphasize their pH nature. The concurrent occurrence of mitopHlashes and $\Delta\psi_m$ drops reflects bursts of concomitant and opposite changes in the electrical and chemical components of the proton-driving force which, depending on the net effect, might impact mitochondrial ATP production and hence cellular bioenergetics.

MitopHlashes have been detected in all eukaryotic species examined so far, from worms to humans (Pouvreau, 2010; Shen et al., 2014; W. Wang et al., 2008; X. Wang et al., 2012; Wei et al., 2011) and were shown to require the integrity of the electron transport chain (Santo-Domingo, Giacomello, Poburko, Scorrano, & Demaurex, 2013; W. Wang et al., 2008; Wei et al., 2011). MitopHlashes require the assembly of functional respiratory chain complexes driven by the protein optic atrophy 1 (OPA1; Rosselin et al., 2017) and can be artificially evoked by photolysis of protons within the matrix (X. Wang et al., 2016) or by imposed depolarization of mitochondria (Santo-Domingo et al., 2013), but their physiological trigger is unknown. MitopHlashes were proposed to be triggered by transient opening of the mitochondrial permeability transition pore (Y. Hou, Mattson, & Cheng, 2013; Li et al., 2012; W. Wang et al., 2008), by the opening of a fusion pore between juxtaposed mitochondria (Santo-Domingo et al., 2013), by matrix Ca^{2+} elevations (Hou et al., 2013; 2016), by swelling (Breckwoldt et al., 2014), or by proton leakage through the ATP synthase (X. Wang et al., 2017). MitopHlash frequency is modulated by oxidative or hyperosmotic stress (T. Hou et al., 2013; Pouvreau, 2010; W. Wang et al., 2008) and by changes in the cellular metabolic state (Fang et al., 2011; Ma et al., 2011; Santo-Domingo et al., 2013; Wei et al., 2011), making mitopHlashes biomarkers of mitochondrial energy metabolism (Gong, Liu, Zhang, Sheu, & Wang, 2015; Wei et al., 2011). More recently, mitopHlash frequency was shown to reflect changes in ATP supply and demand (X. Wang et al., 2017). This led to the

reinterpretation of mitopHlashes as reporters of metabolic imbalance that could regulate the ATP set point by allowing futile respiration to dissipate superfluous ATP.

The accumulating evidence-linking mitopHlashes to physiological alterations in mitochondrial bioenergetics prompted us to investigate the structural underpinnings of these dynamic events. To gain insight on the anatomical basis of mitopHlashes, we compared the ultrastructure of flashing and nonflashing mitochondria by correlative light and electron microscopy. By fixing cells immediately after a flashing event, we could unambiguously distinguish flashing from nonflashing mitochondria in fixed samples and use the coordinates of the fluorescent structures to obtain high-resolution tomograms by serial block face focused ion beam scanning electron microscopy (FIB-SEM). Morphometric analysis of the reconstructed volumes revealed that flashing mitochondria were larger with a preserved cristae morphology and formed tubular extensions and more membrane contact sites than nonflashing mitochondria. These data suggest that flashing mitochondria are in a dynamic state of structural remodeling and are bioenergetically competent, indicating that mitopHlashes do not reflect mitochondrial structural damage but physiological mitochondrial responses.

Results

Resolving the Ultrastructure of Flashing Mitochondria

To capture the structure of flashing mitochondria, we optimized the conditions to ensure rapid diffusion of fixative agents in living cells during pH recordings on a confocal microscope. HeLa cells grown on optical polymer 35 mm dishes with an etched grid were transfected with the matrix-targeted pH-sensitive probe mitoSypHer (Poburko & Demaurex, 2012), and mitopHlashes were recorded on a resonant scanner confocal microscope at high temporal resolution. As previously reported, mitopHlashes occurred at a frequency of 1 flash per minute per cell in these conditions. Cells exhibiting repetitive mitopHlashes in defined regions were selected and fixed with 4% paraformaldehyde immediately after the occurrence of a flashing event (Figure 1(a) and (b) and Supplementary Figure 1 and Movie 1). An activity map was generated by subtracting the SypHer images acquired before and at the peak of the flash to highlight the flashing regions, which were superimposed on a fluorescence image acquired shortly after fixation (Figure 1 (c)). Although the fixation procedure induced a slight swelling and fragmentation of mitochondria, overlay of the activity and fluorescence images allowed the flashing regions on mitochondrial structures to be mapped in the fixed cells (Figure 1(c)). The location of the flashing cell within the coverslip grid was then mapped by acquiring fluorescence and bright-field images at lower resolution (Supplementary Figure 1) using the microscope’s stitch function to produce large images that included grid coordinates. The samples were then further fixed with glutaraldehyde and stained and imbedded in Epon for FIB-SEM (Nunes-Hasler et al., 2017). The recorded cells were identified from their coordinates on the coverslip grid visualized using the surface scanning mode as well as from the cellular footprint that could be discerned using the back-scattered electron mode. Approximately 1,200 slices of 5 × 5 nm resolution (x–z) and 10 nm thickness were generated by focused ion beam milling from a 28 μm × 15 μm cellular volume (Figure 2(a) and Supplementary Movie 2). Amira software was

used to align slices and generate three dimensional tomograms, which could then be resliced orthogonally to produce images of the *x*–*y* orientation that matched the fluorescence image (Figure 2(b) and Supplementary Movie 3). As a confocal slice has a resolution of 250 nm in the *x*–*y* plane and ~750 nm in the *z*-plane, a minimum intensity projection of 200 orthogonal slices (at 5 nm resolution) was generated to visualize all electron-dense structures within a 1 μm volume, allowing an extra 250 nm margin of error for the location of the focus plane within the *z* dimension (Figure 3(a)). Fluorescence images containing the flashing activity overlayed on mitochondria (see Figure 1(c)) were mapped onto the minimum projection using MATLAB software to determine the overall location of the EM stack with respect to the fluorescent image (Figure 3(a) to (c)). The software performed the mapping based on manually set control points designating obvious landmarks (e.g., peripheral mitochondria, with no other mitochondria around, or the border with the nucleus). It allowed rotation, translation, and scaling but no other distortions. Segmentation followed by surface mapping of mitochondrial structures was performed on the entire tomogram stack down-sampled to 20 nm resolution (Figure 4(a) to (c), see also “Material and Methods” section). Once the reconstructed volumes were obtained, contiguous three-dimensional (3D) regions were designated as individual objects (mitochondria). These were then classified as flashing or silent individual mitochondria based on the combined examination of the minimum projection/activity overlay (Figure 3(c)), and of a second mapping, using the same MATLAB software, between the active regions from the fluorescence images and an *x*–*y*-oriented snapshot of the 3D reconstructed individually labeled mitochondrial volumes (Figure 3(d)). Coregistration of the flashing regions with mitochondrial structures was also verified by overlaying fluorescent activity images with individual *x*–y EM slices at 10 nm resolution (Supplementary Figure 2). Individual flashing mitochondria were then examined carefully to exclude segmentation ambiguities, and objects that were not completely included in the tomogram were excluded from the further analysis. After manual curation, six flashing mitochondria were unambiguously identified, two in each of the three tomograms, and were numbered sequentially from 1 to 6 (Figure 4(a) to (c)).

Structural Features of Flashing Mitochondria

We then examined whether the flashing mitochondria had distinctive structural features. Morphometric analysis revealed that flashing mitochondria were larger than nonflashing mitochondria but had comparable surface/volume ratios (Figure 4(d)). On average, the flashing mitochondria were 10-fold larger than the nonflashing mitochondria (Figure 4(d)), with one large (>12 μm^3) flashing mitochondria present in each of the three cells examined (Table 1). In contrast, the volume of the three largest nonflashing mitochondria averaged 5.12 μm^3. We then checked the structure and connectivity of the three pairs of flashing mitochondria present in each cell. Figure 5(a) shows the surface map of the large flashing mitochondrion of Cell 1 (1, colored red, 21.4 μm^3), together with its adjacent small flashing mitochondrion (2, colored pink, 0.09 μm^3) and a juxtaposed nonflashing mitochondrion (silent, colored green). The large Mitochondrion 1 exhibited several bead-on-a-string structures, shown at high resolution in Figure 5 (b), Supplementary Figure 3, and Supplementary Movies 4 and 8. These data sets show three long (>1 μm) tubules (arrows) linking three cristae-containing electron-dense coiled structures protruding from the big convoluted Flashing Mitochondrion 1. In contrast, the very small Flashing Mitochondrion 2,

shown at high resolution in Figure 5(c) and Supplementary Movie 5, also assumed a coiled conformation without connection to the big Flashing Mitochondrion 1 and formed an electron-dense contact site with a neighboring silent mitochondrion (Figure 5(c), arrow). Figure 6(a) shows the surface map of the two large juxtaposed flashing mitochondria of Cell 2 (3, colored red, 13.8 μm^3 and 4, colored pink, 3.7 μm^3). The junction between the two large Flashing Mitochondria 3 and 4, shown at high resolution in Figure 6(b) and Supplementary Movie 6, revealed a broken tubular structure loosely linking the two Flashing Mitochondria 3 and 4 (arrow). Figure 7(a) shows the surface map of the two flashing mitochondria of Cell 3 (5, colored pink, 1.5 μm^3 and 6, colored red, 12.6 μm^3) together with a nonflashing mitochondrion that was found to be contiguous with the Flashing Mitochondrion 6 (silent, colored green). As shown at high resolution in Figure 7(b) and Supplementary Movie 7, the membrane of the large Flashing Mitochondrion 6 was continuous with the membrane of the nonflashing mitochondria, with a stricture at the junctional zone (arrow). This structure coregistered with the transition between flashing and nonflashing regions mapped from the live cell imaging data. The junction between the two Flashing Mitochondria 5 and 6, shown at high resolution in Supplementary Figure 4 and Supplementary Movie 8, revealed a faint yet discernible electron-dense structure linking the two Flashing Mitochondria 5 and 6 (arrow). These data reveal a wealth of intricate contacts forming within and between flashing and nonflashing mitochondria.

As the bioenergetic competence of mitochondria relies on respiratory complexes located in intramitochondrial invaginations known as cristae, we next examined the internal structures of mitochondria. For this, cristae were automatically segmented from the previously labeled mitochondria by eroding the outer and inner membranes and then applying a contrast-based thresholding on Amira (Figure 8(a) to (c)). The EM images were examined at high magnification to validate the segmentation procedure and to verify the integrity of cristae, whose shape appeared similar between the different classes of mitochondria. After surface mapping of cristae, the volume occupied by cristae within each mitochondrion was calculated and expressed as a percentage of the mitochondrial volume. This parameter, which reflects the abundance of active respiratory structures, was not different between flashing and silent mitochondria (Figure 8(d)).

Osmium tetraoxide binds preferentially to unsaturated fatty acids (Belazi, Sole-Domenech, Johansson, Schalling, & Sjovall, 2009) and thus the staining intensity, or electron density, of mitochondrial membranes is dependent on their lipid composition. To probe whether differences in lipid composition might exist between flashing and silent mitochondria, we additionally quantified the electron density of mitochondrial membranes. For this, mitochondrial membranes were automatically segmented by dilating the previously labeled mitochondria, to ensure all of the outer mitochondrial membranes were within the regions to be analyzed, and a contrast-based thresholding similar to the cristae analysis was applied. The inverse intensity units were quantified for each mitochondrion such that increased electron density appears as a higher value. We then compared silent versus flashing mitochondria within each cell, as staining intensities varied from cell to cell, but were relatively homogeneous within each cell. We did not observe any differences in electron density between flashing and silent mitochondria, regardless of whether mitochondria were matched for size or not (Figure 8(e)).

Next, we quantified the frequency of contacts sites between membranes emanating from flashing and non-flashing mitochondria. Contact sites were defined as sites of close apposition (<10 nm) between the outer mitochondrial membrane and the membrane of another membrane-bound structure connected to the same (internal) or to another (external) mitochondrion identified by the segmentation algorithm. Except for the very small Flashing Mitochondrion 2 from Cell 1, five of the six flashing mitochondria formed internal contact sites. The fraction of mitochondrial membrane engaged in internal contacts sites was significantly higher in flashing than in silent mitochondria (Figure 9(d), upper panel) and correlated with the mitochondrial volume (Tables 1 and 2). In contrast, contacts between two different mitochondria occurred at similar frequencies for flashing and silent mitochondria (Figure 9(d), lower panel). This indicates that mitochondrial protrusions come into close contact with themselves in large convoluted mitochondria (Figure 9(a) and (b), arrows). The numerous internal membrane contact sites of the largest Flashing Mitochondrion 1 can be appreciated on the reconstructed mitochondrial volume (Figure 9(c) and Supplementary Movie 10).

Discussion

In this study, we resolve the ultrastructure of flashing mitochondria using correlative light and electron microscopy. To our knowledge, this is the first time that a transient functional event occurring in a defined subcellular structure is correlated morphologically with its ultrastructural underpinnings. This provides proof of principle that the methodology can be used to capture the structure of organelles in their active state. Besides this methodological advance, our study provides new insights on the nature of the elusive mitopHlashes. First, we found that flashing mitochondria were larger than silent mitochondria but had similar surface to volume ratios. This implies that flashing mitochondria have less compact shapes than silent mitochondria, as the surface to volume ratio of compact objects decreases with increasing volume. Indeed, our tomograms indicate that the increased volume of flashing mitochondria does not reflect the linear expansion in the three dimensions of compact objects. Rather, it reflects the accretion of multiple objects, joined by tubular extensions, into polymorphic entities that are less compact than a typical mitochondrion. Second, flashing mitochondria had morphologically intact cristae that occupied a fraction of the mitochondrial volume comparable to nonflashing organelles, indicating that their respiratory apparatus is structurally preserved. Finally, flashing mitochondria were connected by tubular structures and formed more membrane contact sites with themselves. The tubular extensions resembled the mitochondrial nanotunnels reported in immobilized mitochondria, double-membrane protrusions 40 to 200 nm in diameter and up to 30 μm in length (Vincent, Turnbull, Eisner, Hajnoczky, & Picard, 2017). Whether these tubular extensions are constrictions sites related to mitochondrial fusion or fission sites or to mitochondrial swelling is unclear, but the existence of these structures suggests that flashing mitochondria are in a more dynamic state.

These data indicate that flashing mitochondria are structurally intact, maintain respiratory competence, and form self-directed membrane contacts possibly engaged in organelle fusion or fission. MitopHlashes therefore do not reflect an irreversible structural damage of mitochondria due to organelle swelling or to the loss of membrane integrity, as can be

observed under stress conditions. This observation is important because the frequency of mitochondrial flashing is directly correlated with the degree of cellular stress incurred during ionic, osmotic, or redox stress conditions (Feng, Liu, Hou, Wang, & Cheng, 2017). Instead, the preserved cristae structures of flashing mitochondria indicate that mitopHlashes are physiological mitochondrial responses. This confirms the notion that mitopHlashes are bioenergetics responses to sudden drops in mitochondrial potential, in line with our previous observation that imposed depolarizations can evoke mitopHlashes in permeabilized cells (Santo-Domingo et al., 2013). Although circumstantial, our observation that a flashing mitochondrion was connected to a nonflashing mitochondrion at a constriction site provides ultrastructural evidence that flashing events could be mechanistically related to the mitochondrial fusion/fission process. It would be informative to establish whether profusion or profission proteins accumulate around internal membrane contact sites in flashing mitochondria.

Several studies have connected mitopHlashes or their associated drops in mitochondrial membrane potential with transient mitochondrial swelling events detected with matrix-targeted fluorescent proteins (Breckwoldt et al., 2014; Cho et al., 2017; Lee & Yoon, 2014). We also observed that elongated mitochondria transiently adopt a bead-on-string conformation during mitopHlashes (Santo-Domingo et al., 2013) suggesting that, in addition to changes in membrane potential and matrix pH, morphological changes are an intrinsic and possibly causative component of flashing events. Our observation that the large Flashing Mitochondrion 1 exhibits tubular extensions linking swollen mitochondrial structures provides ultrastructural evidence that the flashing events might be associated with transient mitochondrial swelling events. We likely missed transient swelling events in Cells 2 and 3 that were fixed several seconds later (7–8 seconds after the flashing event, Table 1), an interval sufficient for the completion of the swelling event considering the time required for the fixative agents to immobilize cellular structures. Whether or not swelling events cause mitopHlashes remain to be established, but our findings that flashing mitochondria are structurally preserved indicate that the associated morphological changes are fully reversible. A very recent study has associated similar transient swelling events, caused by osmotic movement of water molecules into the mitochondrial matrix driven by potassium influx, with constrictions of the mitochondrial inner compartment termed CoMIC (Cho et al., 2017). The constrictions were dependent on OPA1 cleavage but not on OPA1 fusogenic activity, while we previously reported that OPA1 is required for mitopHlash generation independently of its fusogenic activity and proteolytic state (Rosselin et al., 2017). CoMICs were proposed to reflect dynamic interactions between the inner and outer mitochondrial membranes during mitochondrial fission initiated by overlapping activity with M-AAA protease (OMA1)-dependent cleavage of OPA1 to sOPA1, which destabilizes the mitochondrial contact site and cristae organizing system (MICOS) complex protein Mic60 that tethers the outer and inner mitochondrial membrane (Cho et al., 2017). CoMIC and mitopHlashes are thus both related to the fusion/fission process via OPA1 proteins, with CoMIC but not mitopHlashes associated with OPA1 cleavage. We propose the following mechanism to reconcile these observations: (a) In healthy mitochondria, OPA1 stabilizes cristae junctions and maintains respiratory competency, enabling mitopHlashes to be generated by drops in membrane potential induced by transient openings of high-

conductance pores during membrane fission or fusion events. The increased matrix pH during a mitopHlash preserves the proton-motive force, preventing OMA1-dependent OPA1 cleavage. (b) In mitochondria with failing respiratory complexes or supercomplexes, mitopHlashes cannot be generated during drops in $\Delta\psi_m$, and the loss of the proton-motive force promotes OPA1 cleavage, disrupting Mic60-mediated tethering and initiating fission. In this model, mitopHlashes are compensatory events that preserve the proton-motive force during transient drops in membrane potential, delaying the initiation of mitochondrial fission and of selective mitophagy (Twig et al., 2008).

In summary, we report here the ultrastructural features of mitochondria undergoing spontaneous matrix pH elevations known as mitopHlashes. When chemically fixed 2 to 8 seconds after a flashing event, flashing mitochondria were 10-fold larger than silent mitochondria but retained an intact double membranes and a normal cristae-to-mitochondrial volume. The salient findings were the increased occurrence of internal membrane contacts within flashing mitochondria, with one exhibiting connecting tubules and another connected to a nonflashing mitochondrion by a narrow neck. These findings indicate that mitopHlashes are dynamic, fully reversible events that do not permanently impact the mitochondrial architecture. Flashing mitochondria are bioenergetically competent and appear to be engaged in fusion or fission events. We therefore propose that mitopHlashes reflect transient openings of high-conductance pores during membrane fission or fusion events.

Material and Methods

Cell Lines, Transfection and Media

HeLa cells were cultured in modified Eagle's medium- + glutamax (Gibco, 41090-028) supplemented with 10% fetal bovine serum, 1% penicillin, and 1% streptomycin. Cells were seeded and grown on 35-mm optical polymer-bottom dishes containing an etched grid (35 mm Grid-500 dishes, Ibidi, Switzerland) and transfected with 5 μl Lipofectamine 2000 (Thermo) and 2 μg mitoSypHer (Poburko & Demaurex, 2012). Cells were imaged in a modified Ringer's solution containing 20 mM N-2-hydroxyethylpiperazine-N′-2-ethane sulfonic acid, 140 mM NaCl, 5 mM KCl, 1 mM $MgCl_2$, 2 mM $CaCl_2$, 10 mM glucose, pH set to 7.4 at 37°C.

Ratiometric pH Imaging

Images were acquired on a Nikon A1R inverted confocal microscope with a ×60 objective (oil; CFI Plan APO 1.4 NA), and typically one image was acquired every 1 second. Time-resolved pH imaging was performed at 37°C on cells transiently transfected with mitosypHer (Poburko & Demaurex, 2012). Images were acquired using alternate 440/488 nm laser excitation and 520/535 emission filters. The frequency of pH flashes was analyzed using ImageJ.

Correlation Light Electron Microscopy

Cells displaying repeated mitopHlashing activity were recorded live, and an equal volume of 8% paraformaldehyde/phosphate-buffered saline (4% final concentration) was added manually immediately after a flashing event was detected. A high-resolution image using the

laser-scanning mode was then acquired to document the morphology of the fixed cell. Fluorescence and bright-field images were then acquired using a 40× lens, and the multipoint stitch function was used to capture a 10 × 10 field image that encompassed the grid coordinate markings. Once the grid coordinates were recorded, the dish was removed from the confocal, washed in phosphate-buffered saline, then fixed in 2.5% glutaraldehyde/2% paraformaldehyde in 2 mM $CaCl_2$ in 0.15 M sodium cacodylate buffer (pH 7.4; Ca-Caco) for 3 hours on ice and washed 5× in cold Ca-Caco. With the aid of an inverted bright-field microscope and a 4× objective lens (Zeiss), a square of ~0.5 cm × 0.5 cm was then drawn with a diamond knife around the approximate grid coordinates of the recorded cell. The dish was then stained and embedded for FIB-SEM imaging as previously described (Nunes-Hasler et al., 2017). Once the Epon was hardened, dishes were cut according to the diamond knife markings and the polymer coverslip was dissolved in xylol for 1 hour, or until all of the polymer was removed and the grid etching could be discerned on the surface. The entire large block was then fixed grid-side up to an aluminum pin using Pelco C100 cyanoacrylate glue and Pelco conductive silver paint (Ted 583 Pella, USA), ensuring that silver paint covered the sides of the block all the way to the grid surface to ensure good conductivity from the surface, and avoid charging during EM imaging. Samples were sputter-coated with gold for 30 seconds using a Q150T ES coater (Quorum Technologies, UK). FIB-SEM imaging was performed on a Helios NanoLab G3 microscope (FEI, Netherlands). Grid coordinates were visualized using the low-resolution scanning electron mode at 2 kV/0.2 nA. The cellular footprints were then visualized using the back-scatter electron mode at 15 kV/0.8 nA, and the recorded cell was located by comparing the cellular patterns to the fluorescence and bright-field images. The 28 × 15 μm region to be imaged was then protected by first depositing a 200 nm platinum layer using the electron beam at 2 kV/1.6 nA, followed by a 1.5 μm platinum layer using the ion beam at 30 kV/0.43 nA. Front and side trenches were milled to a depth of 3 μm using the ion beam at 30 kV/21 nA. A primary fiducial for ion beam alignment composed of a 13 × 13 μm platinum square deposited with the ion beam at 30 kV/0.43 nA and a 1 μm-thick, 3-μm-deep *X* milled in the middle was prepared immediately behind the imaging region. A secondary fiducial for block-face alignment was then prepared by milling two 1.5-μm-deep parallel lines separated by 2 μm which were then covered with a 4 × 15 μm, 1-μm-thick layer of carbon deposited using the ion beam at 30 kV/0.23 nA. Images were acquired at the highest resolution setting, resulting in 5 × 5 nm pixels, using the electron beam at 2 kV/0.4 nA, and milling sections with the ion beam at 30kV/2.5 nA every 10 nm using the Autoslice and View software (FEI).

Image Analysis

Drift correction and alignment were performed using Amira software. Orthogonal slices and minimum projections were generated from the aligned stack using ImageJ. For segmentation and mitochondrial 3D surface reconstruction, the original aligned stack was down-sampled by a factor of 4 to limit computation time. A median filter was applied to the stacks. To measure the mitochondrial surface and volume, a semiautomatic segmentation was applied by filling each individual mitochondrion with a paint—and brush—tool in Amira software and by interpolating the mitochondrial contour every five slices. A total of 167 mitochondria were segmented. The 3D reconstruction was obtained using the *generate surface* tool. To identify which mitochondria were flashing, the fluorescence image of the fixed cell (with a

resolution of approximately 250 nm in *x*–*y* and 750 nm in *z*) with the superimposed activity map (see Figure 1(c) and Figure 3(a) to (c)) was overlayed on a minimum projection of 200 *x*–*y*-oriented electron micrographs (equivalent to 1 μm at 5 nm per slice) giving a margin of error in the *z* dimension of approximately ±125 nm. This overlay was performed using a custom MATLAB software script. The activity map was additionally overlayed on a snapshot of the 3D reconstructed mitochondria using the same MATLAB software (Figure 3(d), see also "Results" section). Electron density measurements were performed on down-sampled stacks without a median filter (see also "Results" section). The area 3D and volume 3D parameters corresponding to the mitochondrial surface and volume were analyzed. To segment cristae, the mitochondrial volumes were reduced using double erosion, with first a line in 3D followed by a disk on the *xy* planes, to eliminate the outer and inner membranes, and the reduced volumes were used as a mask on the corresponding down-sampled stacks. The cristae were then delineated with a contrast-based thresholding to select only the electron-dense membrane. The cristae surface was then determined for each mitochondrion. To segment contact sites, the contact sites between mitochondria or within the same mitochondrion were drawn manually on each slice for all the flashing mitochondria and for the nine largest silent mitochondria. An internal morphological gradient (Size 3) was used to skeletonize the segmented mitochondrial surfaces, and this was superimposed onto the manually drawn contact sites to fine-tune contact site areas. The contact sites were finally masked with the labeled mitochondria, and their surface was calculated for each mitochondrion. The segmented objects were overlaid on the EM tomograms by creating slices painted with the color-wash function, set to an alpha transparency of .8.

Supplementary Material

Refer to Web version on PubMed Central for supplementary material.

Funding

The author(s) disclosed receipt of the following financial support for the research, authorship, and/or publication of this article: This work was supported by Schweizerischer Nationalfonds zur Förderung der Wissenschaftlichen Forschung (Award ID: 31003A-149566).

References

Belazi D, Sole-Domenech S, Johansson B, Schalling M, Sjovall P. Chemical analysis of osmium tetroxide staining in adipose tissue using imaging ToF-SIMS. Histochemistry and Cell Biology. 2009; 132:105–115. [PubMed: 19319557]

Breckwoldt MO, Pfister FM, Bradley PM, Marinkovic P, Williams PR, Brill MS, et al. Misgeld T. Multiparametric optical analysis of mitochondrial redox signals during neuronal physiology and pathology in vivo. Nature Medicine. 2014; 20:555–560.

Cho B, Cho HM, Jo Y, Kim HD, Song M, Moon C, et al. Sun W. Constriction of the mitochondrial inner compartment is a priming event for mitochondrial division. Nature Communications. 2017; 8:15754.

Fang H, Chen M, Ding Y, Shang W, Xu J, Zhang X, et al. Cheng H. Imaging superoxide flash and metabolism-coupled mitochondrial permeability transition in living animals. Cell Research. 2011; 21:1295–1304. [PubMed: 21556035]

Feng G, Liu B, Hou T, Wang X, Cheng H. Mitochondrial flashes: Elemental signaling events in eukaryotic cells. Handbook of Experimental Pharmacology. 2017; 240:403–422. [PubMed: 28233181]

Gong G, Liu X, Zhang H, Sheu SS, Wang W. Mitochondrial flash as a novel biomarker of mitochondrial respiration in the heart. American Journal of Physiology- Heart and Circulatory Physiology. 2015; 309:H1166–H1177. [PubMed: 26276820]

Hou T, Jian C, Xu J, Huang AY, Xi J, Hu K, et al. Wang X. Identification of EFHD1 as a novel Ca^{2+} sensor for mitoflash activation. Cell Calcium. 2016; 59:262–270. [PubMed: 26975899]

Hou T, Zhang X, Xu J, Jian C, Huang Z, Ye T, et al. Cheng H. Synergistic triggering of superoxide flashes by mitochondrial Ca^{2+} uniport and basal reactive oxygen species elevation. The Journal of Biological Chemistry. 2013; 288:4602–4612. [PubMed: 23283965]

Hou Y, Mattson MP, Cheng A. Permeability transition pore-mediated mitochondrial superoxide flashes regulate cortical neural progenitor differentiation. PLoS One. 2013; 8:e76721. [PubMed: 24116142]

Lee H, Yoon Y. Transient contraction of mitochondria induces depolarization through the inner membrane dynamin OPA1 protein. The Journal of Biological Chemistry. 2014; 289:11862–11872. [PubMed: 24627489]

Li K, Zhang W, Fang H, Xie W, Liu J, Zheng M, et al. Cheng H. Superoxide flashes reveal novel properties of mitochondrial reactive oxygen species excitability in cardiomyocytes. Biophysical Journal. 2012; 102:1011–1021. [PubMed: 22404923]

Ma Q, Fang H, Shang W, Liu L, Xu Z, Ye T, et al. Cheng H. Superoxide flashes: Early mitochondrial signals for oxidative stress-induced apoptosis. The Journal of Biological Chemistry. 2011; 286:27573–27581. [PubMed: 21659534]

Mitchell P. Coupling of phosphorylation to electron and hydrogen transfer by a chemi-osmotic type of mechanism. Nature. 1961; 191:144–148. [PubMed: 13771349]

Nunes-Hasler P, Maschalidi S, Lippens C, Castelbou C, Bouvet S, Guido D, et al. Demaurex N. STIM1 promotes migration, phagosomal maturation and antigen cross-presentation in dendritic cells. Nature Communications. 2017; 8(1):1852.

Poburko D, Demaurex N. Regulation of the mitochondrial proton gradient by cytosolic Ca^{2+} signals. Pflügers Archiv-European Journal of Physiology. 2012; 464:19–26. [PubMed: 22526460]

Pouvreau S. Superoxide flashes in mouse skeletal muscle are produced by discrete arrays of active mitochondria operating coherently. PLoS One. 2010; 5:e13035. [PubMed: 20927399]

Rosselin M, Santo-Domingo J, Bermont F, Giacomello M, Demaurex N. L-OPA1 regulates mitoflash biogenesis independently from membrane fusion. EMBO Reports. 2017; 18:451–463. [PubMed: 28174208]

Santo-Domingo J, Giacomello M, Poburko D, Scorrano L, Demaurex N. OPA1 promotes pH flashes that spread between contiguous mitochondria without matrix protein exchange. The EMBO Journal. 2013; 32:1927–1940. [PubMed: 23714779]

Schwarzlander M, Wagner S, Ermakova YG, Belousov V, Radi R, Beckman JS, et al. Murphy MP. The ‘mitoflash’ probe cpYFP does not respond to superoxide. Nature. 2014; 514:E12–E14. [PubMed: 25341790]

Shen EZ, Song CQ, Lin Y, Zhang WH, Su PF, Liu Y, et al. Dong MQ. Mitoflash frequency in early adulthood predicts lifespan in *Caenorhabditis elegans*. Nature. 2014; 508:128–132. [PubMed: 24522532]

Twig G, Elorza A, Molina AJ, Mohamed H, Wikstrom JD, Walzer G, et al. Shirihai OS. Fission and selective fusion govern mitochondrial segregation and elimination by autophagy. The EMBO Journal. 2008; 27:433–446. [PubMed: 18200046]

Vincent AE, Turnbull DM, Eisner V, Hajnoczky G, Picard M. Mitochondrial nanotunnels. Trends in Cell Biology. 2017; 27:787–799. [PubMed: 28935166]

Wang W, Fang H, Groom L, Cheng A, Zhang W, Liu J, et al. Cheng H. Superoxide flashes in single mitochondria. Cell. 2008; 134:279–290. [PubMed: 18662543]

Wang X, Jian C, Zhang X, Huang Z, Xu J, Hou T, et al. Cheng H. Superoxide flashes: Elemental events of mitochondrial ROS signaling in the heart. Journal of Molecular and Cellular Cardiology. 2012; 52:940–948. [PubMed: 22405973]

Wang X, Zhang X, Huang Z, Wu D, Liu B, Zhang R, et al. Cheng H. Protons trigger mitochondrial flashes. Biophysical Journal. 2016; 111:386–394. [PubMed: 27463140]

Wang X, Zhang X, Wu D, Huang Z, Hou T, Jian C, et al. Cheng H. Mitochondrial flashes regulate ATP homeostasis in the heart. eLife. 2017; 6:e23908. [PubMed: 28692422]

Wei L, Salahura G, Boncompagni S, Kasischke KA, Protasi F, Sheu SS, Dirksen RT. Mitochondrial superoxide flashes: Metabolic biomarkers of skeletal muscle activity and disease. FASEB Journal. 2011; 25:3068–3078. [PubMed: 21646399]

Europe PMC Funders Author Manuscripts

Europe PMC Funders Author Manuscripts

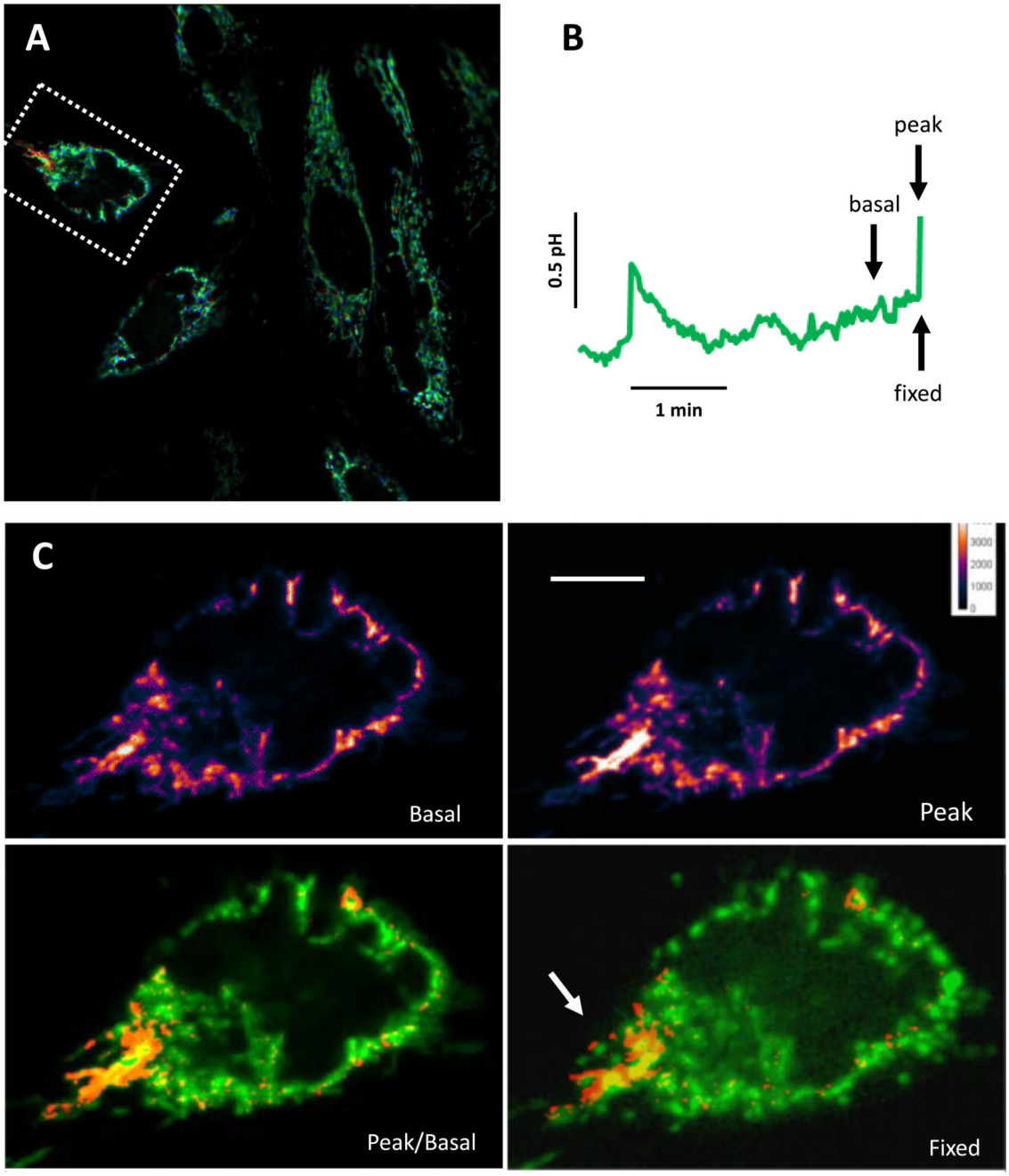

Figure 1. Mapping flashing mitochondria.

(a) Spontaneous matrix pH elevations recorded by confocal microscopy in HeLa cells expressing mitoSypHer ($\lambda_{ex}/\lambda_{em}$=488/520 nm). Dotted line indicates a cell exhibiting repetitive mitopHlashes. See also Supplementary Movie 1. (b) Time-resolved fluorescence recording of the cell highlighted in panel (a). Fixative agents were added immediately after the second flashing event (arrow). (c) Images acquired before (basal) and during the mitopHlash event (peak) were subtracted (peak–basal) and the active regions (orange,

pointed by arrow) superimposed on the image acquired immediately after the addition of fixative agents (fixed). Bar: 10 μm.

Europe PMC Funders Author Manuscripts

Europe PMC Funders Author Manuscripts

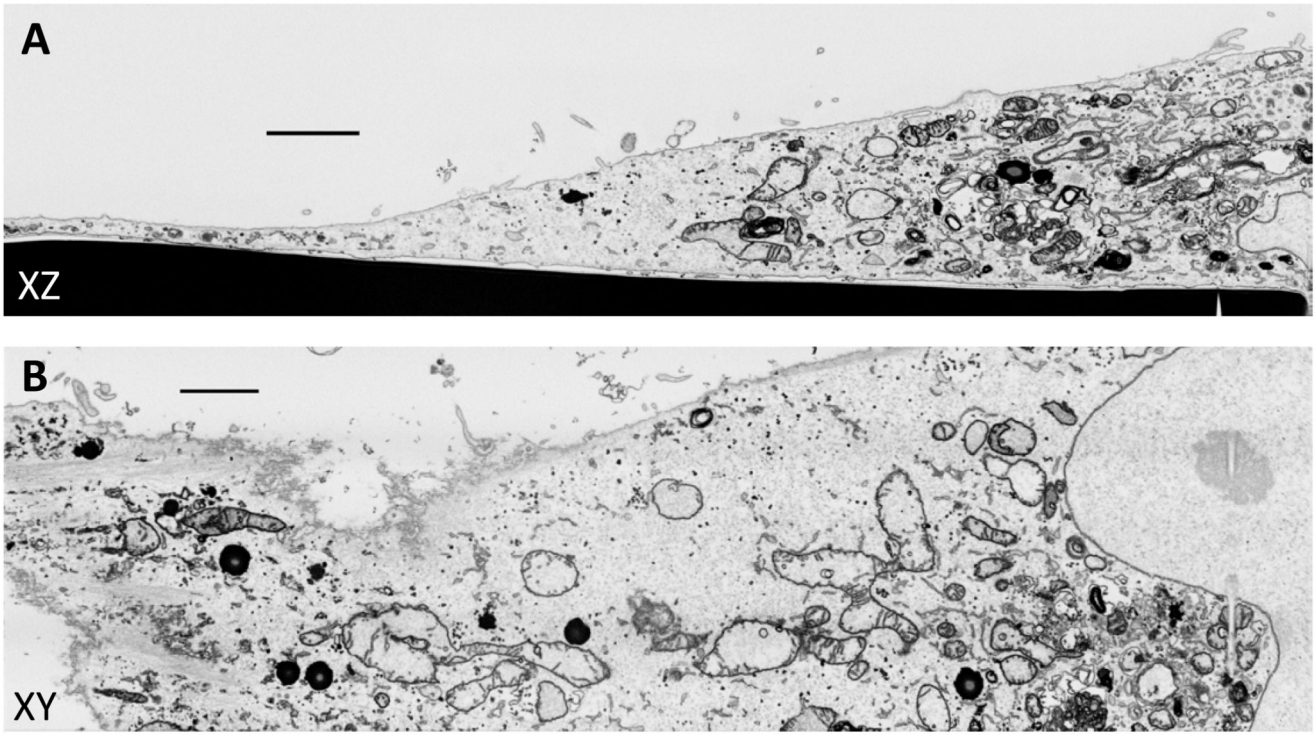

Figure 2. Electron tomogram of flashing mitochondria.

(a) Tomogram generated by serial block face FIB-SEM from the active region in Figure 1. The top image of a 600-image stack from a 28 μm × 15 μm cellular volume in the *x*–*z* orientation at 5 nm × 5 nm × 10 nm resolution is shown. Full tomogram in Supplementary Movie 2. (b) Tomogram resampled orthogonally in the *x*–*y* orientation at 10 nm × 10 nm × 5 nm resolution to match the orientation of the fluorescence image. The top image of a 200-image stack is shown. Full tomogram in Supplementary Movie 3. Bars: 1 μm.

Europe PMC Funders Author Manuscripts

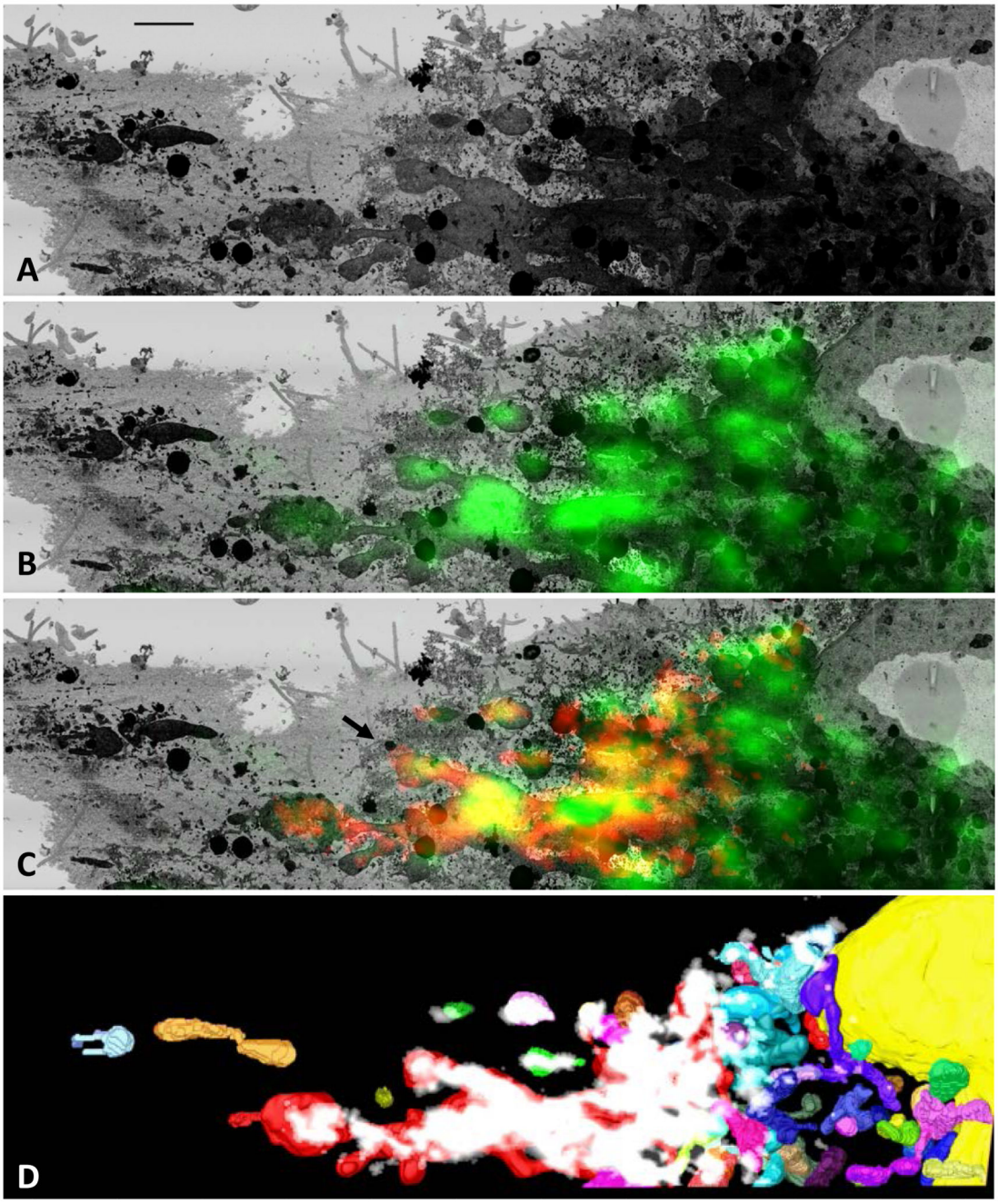

Figure 3. Correlative light and electron microscopy.

(a) Minimum intensity projection of the image stack shown in Figure 2 (b). Mitochondria appear as large interconnected electron-dense structures. (b) Overlay of the fluorescence image of fixed cells on the tomogram projection using MATLAB software. (c) Overlay of the flashing region (red), fluorescence of fixed cells (green), and tomogram projection (gray). Bar: 1 μm. (d) Overlay of a snapshot of the initial, uncurated 3D reconstruction (colored objects) and the flashing region (white).

Europe PMC Funders Author Manuscripts

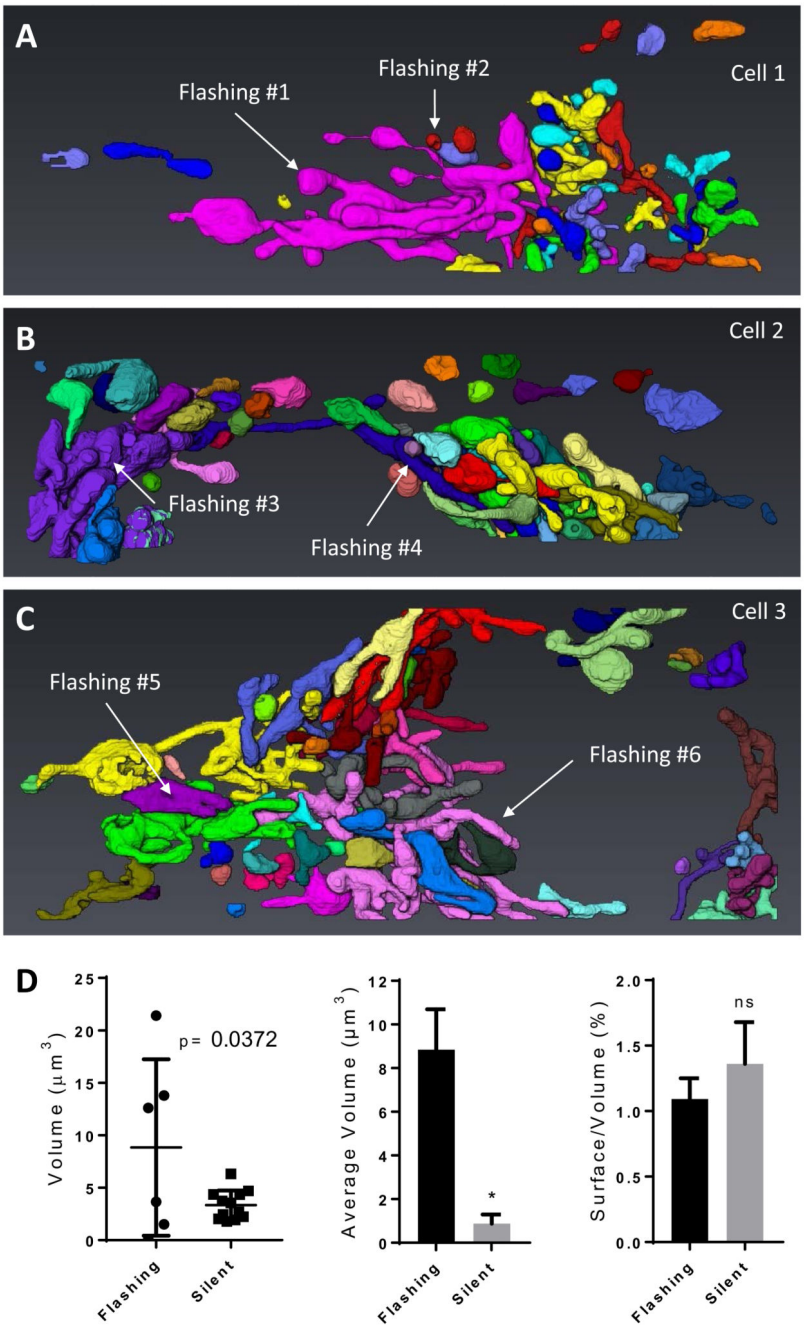

Figure 4. Morphology of flashing and nonflashing mitochondria.

(a–c) Surface map of all mitochondria identified in three tomograms by the segmentation algorithm. Each color represents a single mitochondrion. The six flashing mitochondria, numbered sequentially from Cell 1 to Cell 3 are indicated by arrows. (d) Quantification of the volume of individual mitochondria (left) and of the average volume (center) and surface to volume ratio (right) of the different classes of mitochondria. Values in center and right panels are means ± standard deviation of the average values from the three tomograms

comprising a total of 6 and 156 flashing and silent mitochondria, respectively, *$p = .02$, Welsh's t test.

Europe PMC Funders Author Manuscripts

Europe PMC Funders Author Manuscripts

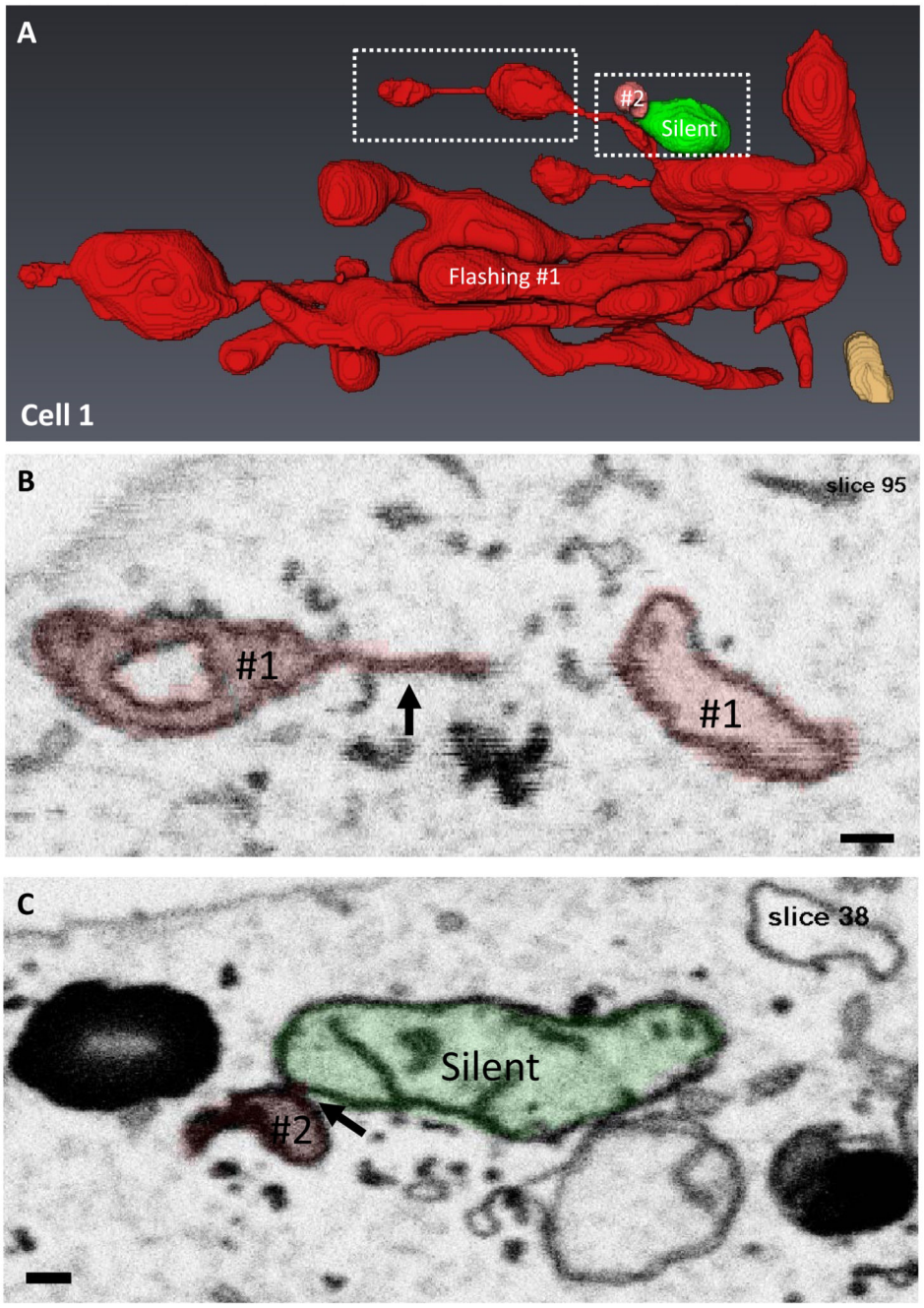

Figure 5. Ultrastructural features of the two flashing mitochondria from Cell 1.

(a) Surface map of the two flashing mitochondria from Cell 1. Flashing mitochondria are colored red (1) and pink (2), a juxtaposed nonflashing mitochondrion is colored green (silent). Dotted lines outline the tomograms sections shown in Supplementary Movies 4 and 5. (b) Tomogram slice illustrating a tubular structure (arrow) linking two parts of the Flashing Mitochondrion 1 from Cell 1, colored in red. Full tomogram in Supplementary Movie 4. (c) Tomogram slice illustrating a contact site (arrow) between Flashing

Mitochondrion 2 from Cell 1 and its juxtaposed nonflashing mitochondrion. Full tomogram in Supplementary Movie 5. Bars: 200 nm.

Europe PMC Funders Author Manuscripts

Europe PMC Funders Author Manuscripts

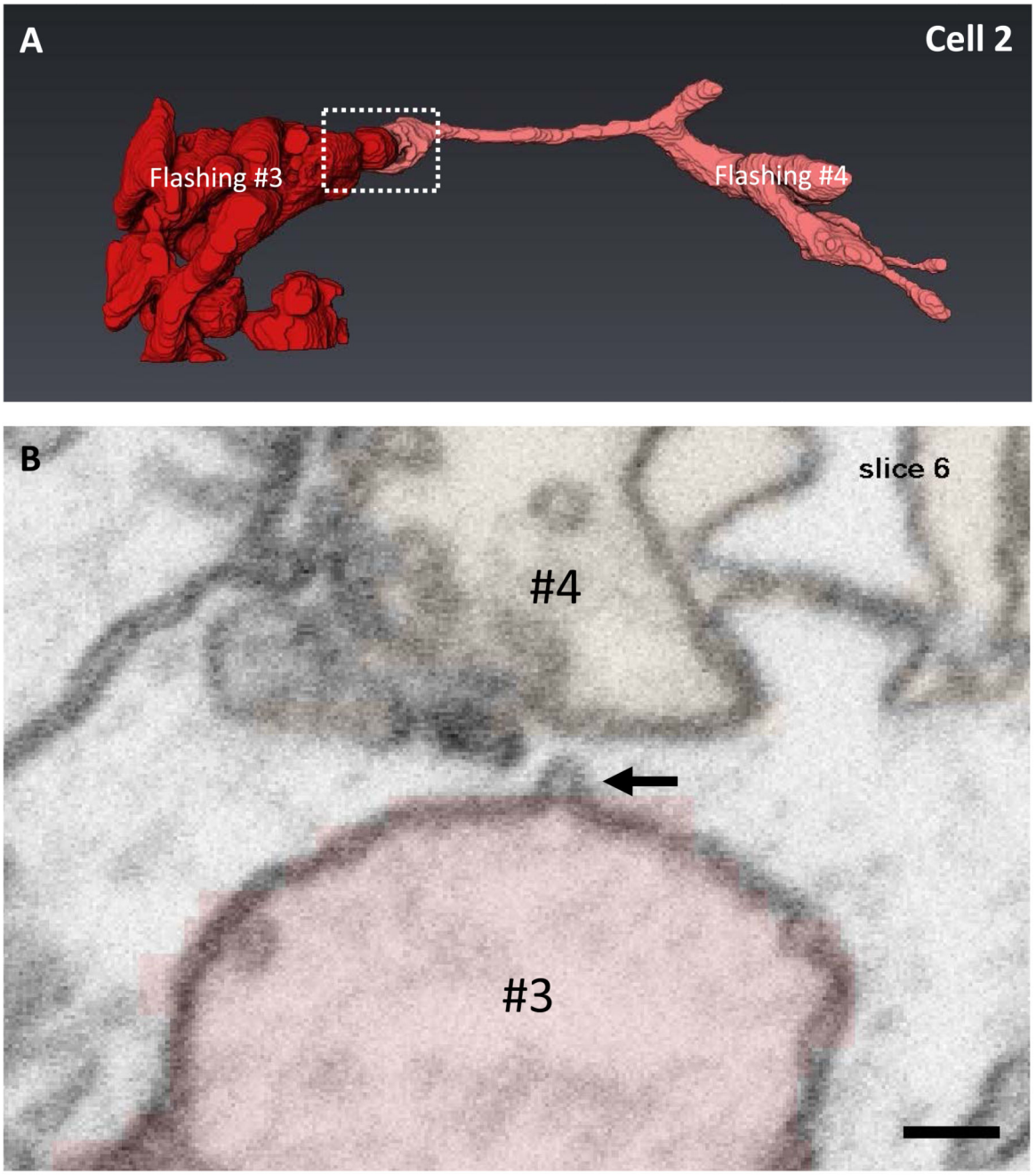

Figure 6. Ultrastructural features of the two flashing mitochondria from Cell 2.

(a) Surface map of the two flashing mitochondria from Cell 2. Flashing mitochondria are colored red (3) and pink (4). Dotted lines outline the tomogram section shown in Supplementary Movie 6. (b) Tomogram slice illustrating a tubular structure (arrow) at the interface between Flashing Mitochondria 3 and 4 from Cell 2. Full tomogram in Supplementary Movie 6. Bar: 200 nm.

Europe PMC Funders Author Manuscripts

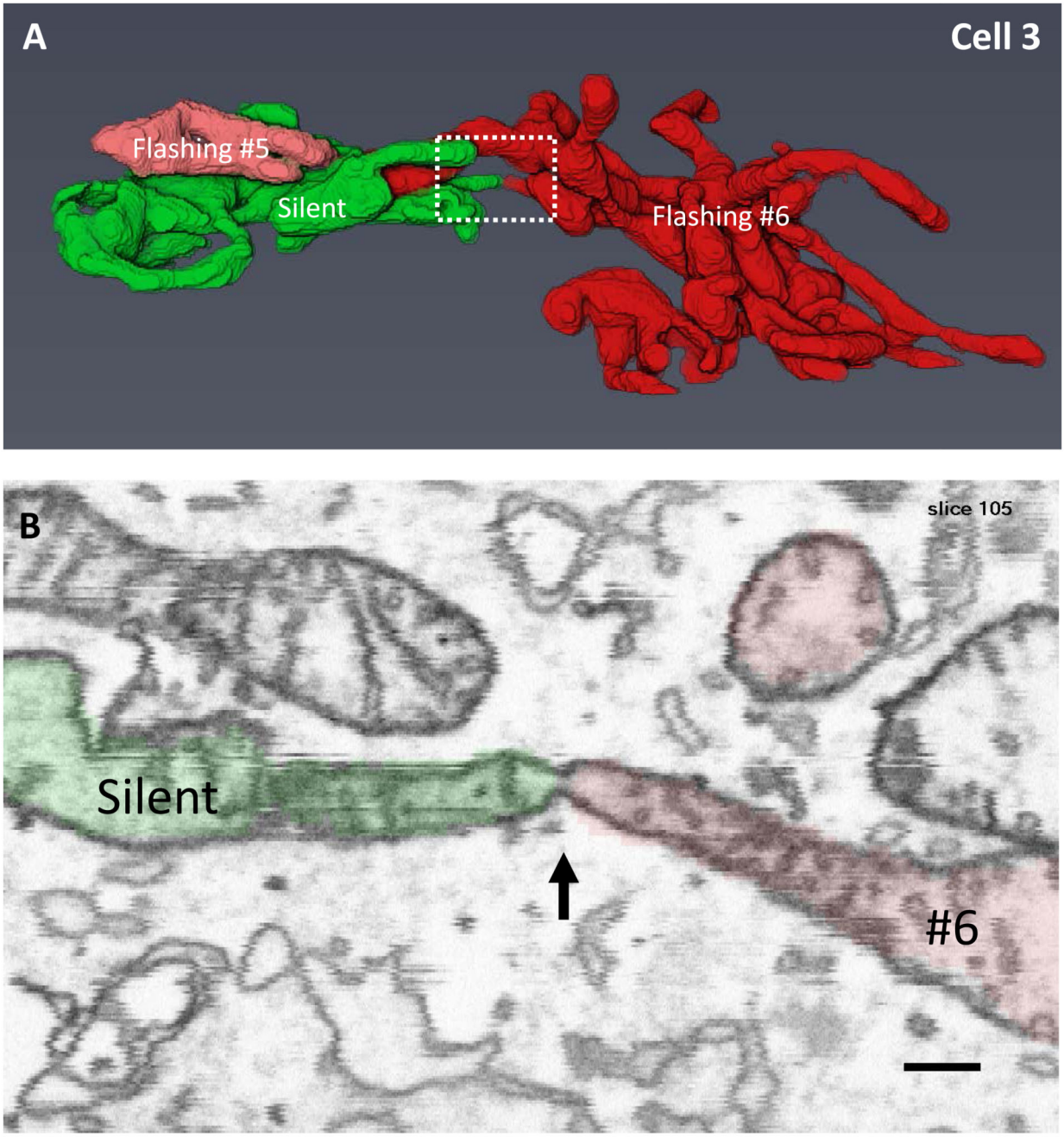

Figure 7. Ultrastructural features of the two flashing mitochondria from Cell 3.

(a) Surface map of the two flashing mitochondria from Cell 3. Flashing mitochondria are colored pink (5) and red (6), a juxtaposed nonflashing mitochondrion is colored green (silent). Dotted lines outline the tomogram section shown in Supplementary Movie 7. (b) Tomogram slice illustrating a junction (arrow) between Flashing Mitochondrion 6 from Cell 3 and a nonflashing mitochondrion. Note the fusion of the mitochondrial membranes. Full tomogram in Supplementary Movie 7. Bar: 200 nm.

Europe PMC Funders Author Manuscripts

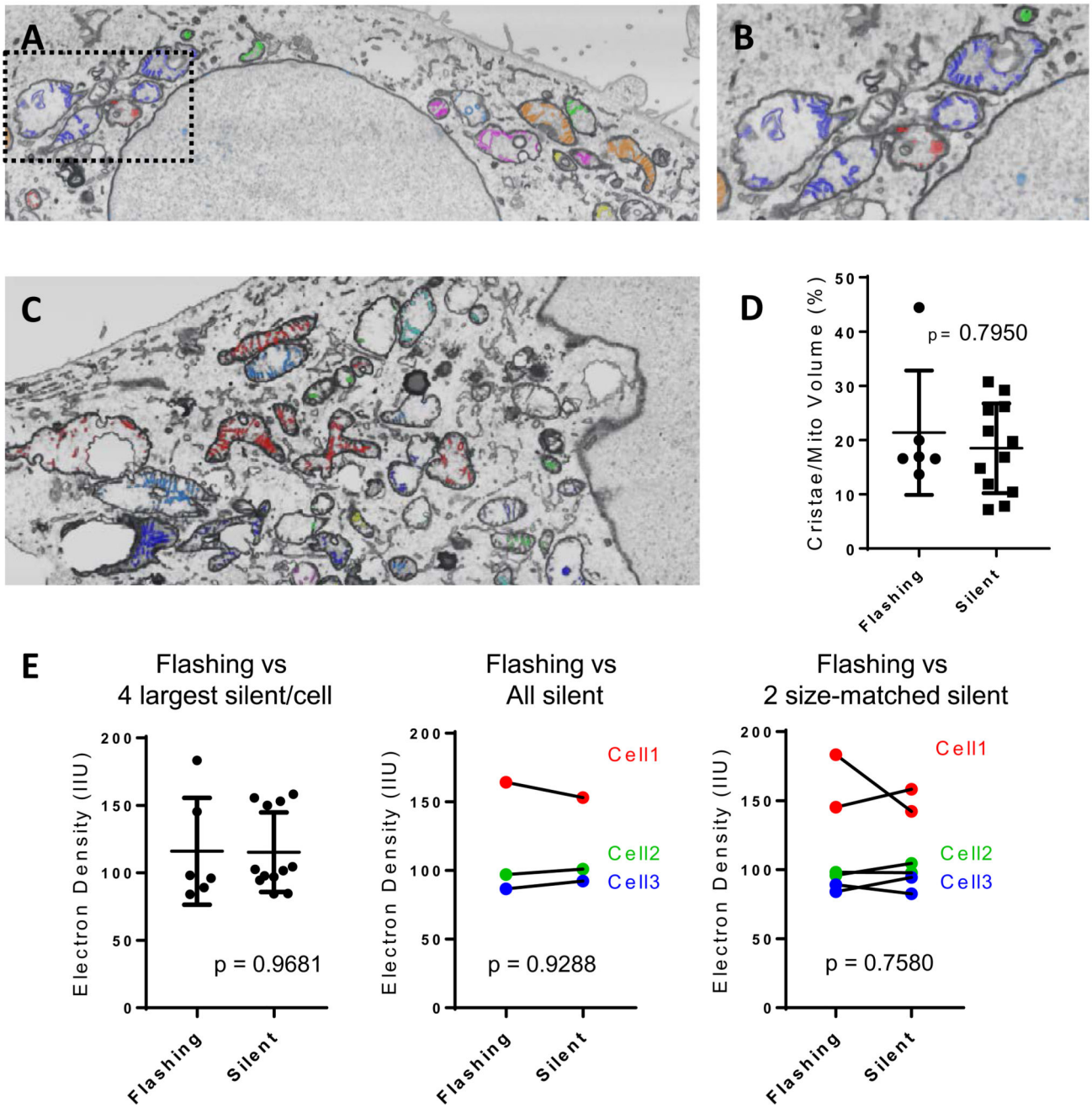

Figure 8. Cristae of flashing and nonflashing mitochondria.

(a–c) EM pictures showing cristae segmentation within individual mitochondria. Each color corresponds to a single mitochondrion. (d) Quantification of the volume of cristae normalized to the total volume of each individual mitochondrion. The four largest silent mitochondria from each tomogram ($n = 12$) were quantified. (e) Quantification of the electron density, measured as IIUs. The left panel shows all flashing mitochondria ($n = 6$) compared with the four largest silent mitochondria from each tomogram ($n = 12$). The middle panel compared the average of all flashing mitochondria within a cell ($n = 2$/cell) to

the average of all silent mitochondria within the same cell (n = 58/53/43 for cells 1/2/3). The right panel compares each flashing mitochondrion within a cell (n = 2/cell) to the silent mitochondrion within the same cells most closely matching it in volume (n = 2/cell). IIU = inverse intensity unit.

Europe PMC Funders Author Manuscripts

Europe PMC Funders Author Manuscripts

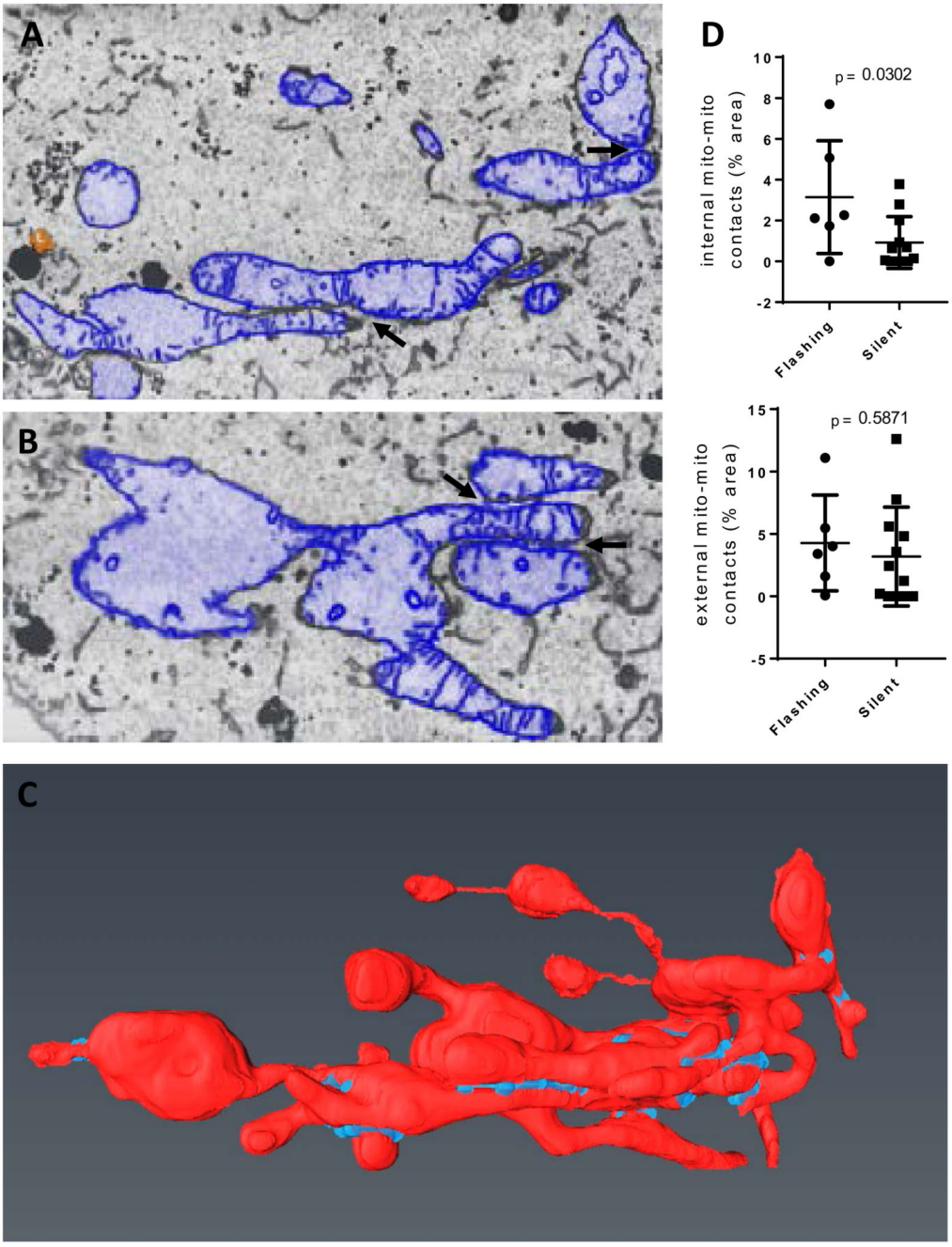

Figure 9. Membrane contacts within Flashing Mitochondrion 1 from Cell 1.

(a and b) EM pictures showing membrane contact sites (arrows) within Flashing Mitochondrion 1 from Cell 1, colored in blue. The contour of the mitochondrion was delineated using an internal morphological gradient (of three pixels) to define a homogenous thickness of membrane for all contact sites. (c) Surface mapping of Flashing Mitochondrion 1 with its internal membrane contact sites highlighted in light blue (arrows). See also Supplementary Movie 8. (d) Quantification of the fraction of mitochondrial membrane

engaged in internal contact sites. The four largest silent mitochondria from each tomogram (n = 12) were analyzed. See also Tables 1 and 2 and Supplementary Movie 10.

Europe PMC Funders Author Manuscripts

Europe PMC Funders Author Manuscripts

Table 1
Morphometric Parameters of Flashing Mitochondria.

	Lag time (s)	Mito No.	Mito volume (μm^3)	Cristae volume (μm^3)	Mito surface (μm^2)	External contacts (μm^2)	Internal contacts (μm^2)
Cell 1	2.28	1	21.4	3.62	161.2	0.10	12.4
		2	0.09	0.04	1.65	0.09	0.00
Cell 2	7.55	3	13.8	1.89	106.2	4.26	2.24
		4	3.66	0.73	40.4	1.37	0.70
Cell 3	7.95	5	12.6	2.09	152	2.45	3.43
		6	1.51	0.25	14.6	1.62	0.74

The interval between the occurrence of the mitopHlash and the chemical fixation is indicated for each of the three cells analyzed (second column). The volume, surface area, and cristae volume of each flashing mitochondrion are indicated as well as the fraction of the outer mitochondrial membrane engaged in contacts with the same (internal) with another (external) mitochondrion. Mito = mitochondria.

Europe PMC Funders Author Manuscripts

Table 2
Morphometric Parameters of Silent Mitochondria.

	Mito No.	Mito volume (μm^3)	Cristae volume (μm^3)	Mito surface (μm^2)	External contacts (μm^2)	Internal contacts (μm^2)
Cell 1	8	4.36	1.14	41.2	2.31	1.15
	27	2.02	0.34	18.9	0.00	0.00
	10	1.92	0.49	13.9	1.08	0.28
	28	1.79	0.14	18.5	0.00	0.01
Cell 2	7	3.74	0.39	30.1	1.45	0.28
	8	2.70	0.83	26.9	0.96	0.00
	10	2.44	0.29	16.1	2.03	0.00
	29	2.23	0.16	16.4	0.00	0.62
Cell 3	4	6.32	1.37	79.4	1.94	0.11
	3	4.69	1.37	69.0	0.85	0.48
	19	4.33	0.64	44.8	0.09	0.00
	5	3.54	0.70	46.6	0.00	0.30

The four largest silent mitochondria from each tomogram were selected for analysis. The volume, surface area, and cristae volume of each mitochondrion are indicated as well as the fraction of the outer mitochondrial membrane engaged in contacts with the same (internal) with another (external) mitochondrion. Mito = mitochondria.